Nanophotonic light management for perovskite–silicon tandem solar cells

Duote Chen
Phillip Manley
Philipp Tockhorn
David Eisenhauer
Grit Köppel
Martin Hammerschmidt
Sven Burger
Steve Albrecht
Christiane Becker
Klaus Jäger

SPIE.

Nanophotonic light management for perovskite–silicon tandem solar cells

Duote Chen,[a,b] Phillip Manley,[a,b] Philipp Tockhorn,[a] David Eisenhauer,[a] Grit Köppel,[a] Martin Hammerschmidt,[b,c] Sven Burger,[b,c] Steve Albrecht,[a] Christiane Becker,[a] and Klaus Jäger[a,b,*]

[a]Helmholtz–Zentrum Berlin für Materialien und Energie GmbH, Berlin, Germany
[b]Zuse Institute Berlin, Berlin, Germany
[c]JCMwave GmbH, Berlin, Germany

Abstract. Currently, perovskite–silicon tandem solar cells are one of the most investigated concepts for overcoming the theoretical limit for the power conversion efficiency of silicon solar cells. For monolithic tandem solar cells, the available light must be distributed equally between the two subcells, which is known as current matching. For a planar device design, a global optimization of the layer thicknesses in the perovskite top cell allows current matching to be reached and reflective losses of the solar cell to be minimized at the same time. However, even after this optimization, the reflection and parasitic absorption losses add up to 7 mA/cm^2. In this contribution, we use numerical simulations to study how well hexagonal sinusoidal nanotextures in the perovskite top-cell can reduce the reflective losses of the combined tandem device. We investigate three configurations. The current density utilization can be increased from 91% for the optimized planar reference to 98% for the best nanotextured device (period 500 nm and peak-to-valley height 500 nm), where 100% refers to the Tiedje–Yablonovitch limit. In a first attempt to experimentally realize such nanophotonically structured perovskite solar cells for monolithic tandems, we investigate the morphology of perovskite layers deposited onto sinusoidally structured substrates. © *The Authors. Published by SPIE under a Creative Commons Attribution 3.0 Unported License. Distribution or reproduction of this work in whole or in part requires full attribution of the original publication, including its DOI.* [DOI: 10.1117/1.JPE.8.022601]

Keywords: numerical approximation and analysis; spectral properties; solar energy.

1 Introduction

Crystalline silicon (c-Si) solar cells have achieved enormous dominance in the photovoltaic market due to their high efficiencies, excellent material quality, and continual reduction in manufacturing costs. The current record efficiency of 26.7%[1] is already 89% of the theoretical limit value for the power conversion efficiency for single-junction solar cells.[2] Further improvement in this technology will become increasingly difficult. However, to further boost the distribution of photovoltaics in the future, higher efficiencies at low costs are required.[3]

We aim to surpass the Shockley–Queisser limit[4]—the most important technological limit for single-junction solar cells—with tandem solar cells, which combine two solar cells with different bandgaps. The incident sunlight first hits the top cell, which has a higher bandgap and harvests the high-energy photons at a higher voltage, whereas the low-energy photons are transferred to the bottom cell, which has a lower bandgap and corresponding lower voltage. In this way, high-energy photons are able to contribute more voltage to the device instead of losing their excess energy by thermalization.

Lead halide perovskite materials have excellent optical properties for tandem applications due to their steep absorption edge[5] and a tunable bandgap.[6,7] As a result, tandem cells with

*Address all correspondence to: Klaus Jäger, E-mail: klaus.jaeger@helmholtz-berlin.de

a perovskite top cell and a silicon bottom cell have the potential to reach efficiencies beyond 30%,[8–10] if optical losses are adequately adressed.[11]

In monolithic (two-terminal) tandem cells, the perovskite top cell and the c-Si bottom cell are electrically connected in series. Hence, for high efficiencies the photocurrent density of the top and bottom cell must be matched. Recently, we numerically maximized the achievable photo-current density for different planar monolithic perovskite-silicon tandem device architectures with antireflective coatings by optimizing the layer thicknesses. The architecture with the electron-selective contact and *n*-doped layers on the front of the perovskite and silicon cells, respectively,[12] enables efficiencies exceeding 30%, when the perovskite bandgap is optimized as well.[13] However, for fully planar devices, reflection losses cause a significant limitation for the matched photocurrent density J_{ph}.

Textured interfaces can reduce reflection losses via (1) enhancing coupling of light into the structure and (2) scattering light such that the average path length in the absorber is increased, leading to increased absorption especially in weakly absorbing regimes. In recent years, much effort has been put into developing two-dimensional (2-D) structures for light trapping.[14–21] For nanostructures, which texture the electrically active layers of the solar cell, it is mandatory that they have no detrimental effect on the electric solar cell performance. Therefore, we decided to focus on hexagonal sinusoidal nanotextures,[22,23] which allow for the combination of a strong antireflective effect with good electrical performance, as we demonstrated for liquid-phase crys-tallized silicon thin-film solar cells.[24,25]

In this work, we investigate how sinusoidal nanotextures affect the optical performance of perovskite–silicon tandem solar cells. To efficiently optimize the perovskite layer thickness for current matching, we use Newton's method. As motivation, we demonstrate the experimental feasibility of spin-coating perovskite layers onto sinusoidally nanotextured substrates.

2 Experimental Motivation

So far, little experimental evidence of nanostructured perovskite layers has been published: in some studies, different nanostructures were imprinted into the perovskite top surface.[26–28] Although these top surface patterning techniques demand postprocessing of the perovskite film after fabrication, other studies report perovskite grown onto different kinds of nanophotoni-cally patterned charge selective layers.[29,30]

Here, we demonstrate how sinusoidally nanotextured films can be fabricated with spin coat-ing. This deposition method is chosen since it has shown to yield the best performing perovskite absorber layers for photovoltaic application so far. As model systems, we use two kinds of glass substrates, which are covered with sinusoidal nanotextures. The periods are $P = 500$ nm and $P = 750$ nm; the respective valley-to-peak heights are $h = 80$ nm and $h = 200$nm, which correspond to aspect ratios of $a = 0.16$ and $a = 0.27$, respectively. The nanotextures were manufactured with nanoimprint lithography using a hybrid polymer with glass-like properties (OrmoComp by Micro Resist Technology GmbH). Details on our nanoimprint lithography process can be found in Ref. 31.

For better imaging capabilities, we thermally evaporate 30 nm of silver onto the nanotextured substrates. In addition, we prepare a flat reference substrate by spin-coating a thin layer of polytriarylamine (PTAA) onto an indium tin oxide (ITO) substrate. PTAA is a common hole transporting material (HTM) in *p-i-n* perovskite solar cells,[32–34] which supports the uniform growth of perovskite.

For the perovskite layer fabrication in our experiment, we use the mixed halide perovskite composition $Cs_{0.05}(FA_{0.83}MA_{0.17})_{0.95}Pb(I_{0.83}Br_{0.17})_3$ using a recipe by Saliba et al.[35]

We spin-coated the as-prepared 0.8-M solution according to the antisolvent method to pro-mote the crystallization into perovskite. This method enables crystallization starting from the top interface of the perovskite[36] film, which allows for the growth of films with a high optoelectronic quality, which is mostly independent of the (nanotextured) substrate.[37]

We investigate the morphology of the perovskite layers with scanning electron microscopy (SEM). Figures 1(a) and 1(b) show cross-sectional SEM images of the perovskite on the two sinusoidal textures with $P = 500(750)$ nm and $a = 0.16(0.27)$. The perovskite films show thicknesses of 420 to 500 nm and 420 to 600 nm on the $P = 500$ nm and $P = 750$ nm
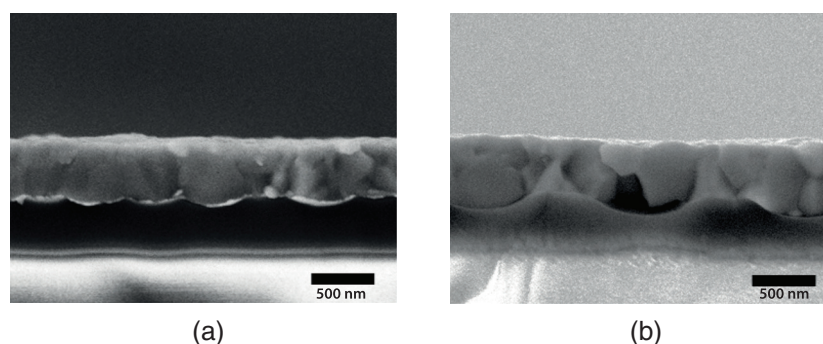
Fig. 1 5 kV SEM micrograph images of perovskite on sinusoidal substrates with (a) $P = 500$ nm and $a = 0.16$, (b) $P = 750$ nm and $a = 0.27$. The bright layer between substrate and perovskite represents the evaporated silver.

nanotextured substrates, respectively. The layers are thicker than those required for good current matching, as we will discuss in Sec. 4 and Table 2. However, they can be easily adjusted by reducing the molarity of the perovskite precursor solution.

The perovskite fills the sinusoidal structures for both periodicities and can compensate a height difference of up to 200 nm on the substrate. On the top surface, the underlying sinusoidal nanotexture is not visible, which is in accordance with crystallization starting from the top surface.

We further investigate the perovskite surface with atomic force microscopy (AFM) measurements. Figure 2(a) shows a top view AFM micrograph (3 μm $\times$ 3 μm) of the bare nanotextured substrate with $P = 500$ nm. The hexagonal arrangement of the sinusoidal structure is clearly visible. In contrast, the 3 μm $\times$ 3 μm micrographs in Figs. 2(b) and 2(c) show the disordered surfaces of perovskite layers on this structured substrate and on (flat) PTAA, respectively. The perovskite films grown on these different substrates have a root mean square (RMS) roughness
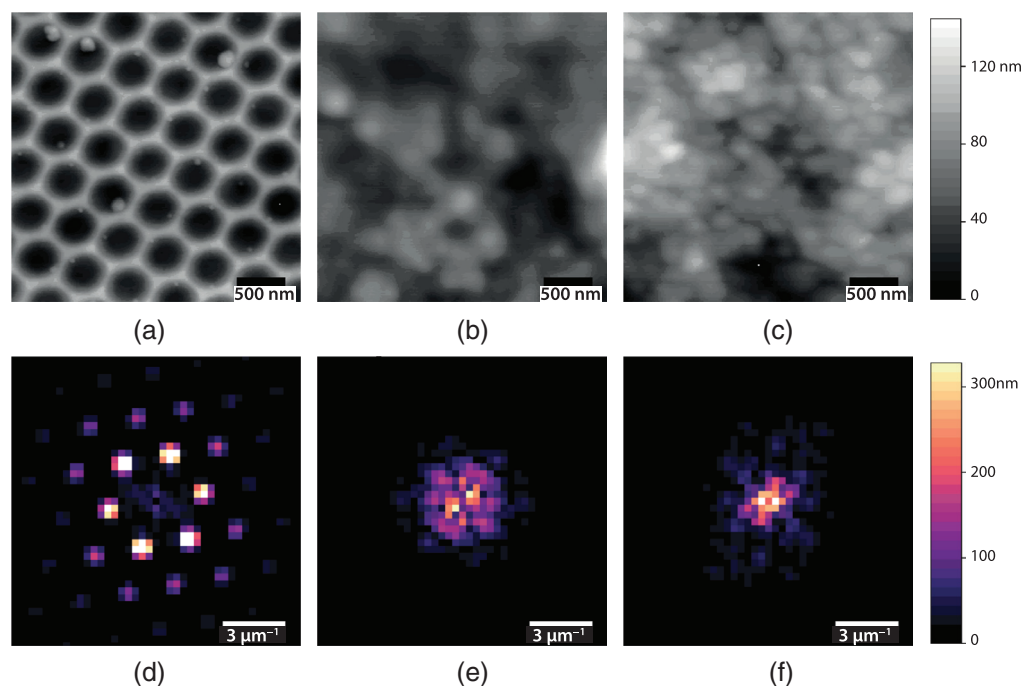

Fig. 2 AFM micrograph images of (a) an uncoated, sinusoidally structured substrate, (b) perovskite on a structured substrate and (c) perovskite on flat PTAA as a reference. (d)–(f) display the 2-D Fourier transforms (FTs) corresponding to (a)–(c).

of 16 and 22 nm for the structured and flat substrates, respectively. The RMS roughness values of the perovskite layers in this study are larger than reported elsewhere,[38,39] which can be attributed to differences in compositions, processing, and substrates.

Figures 2(d)–2(f) show the Fourier transforms (FTs) corresponding to the AFM height profiles from Figs. 2(a)–2(c). The FT of the bare substrate features six hexagonally arranged spots of high intensity around the center and low intensity spots of higher order at larger wavenumbers. In contrast, the FTs of both perovskite layers in Figs. 2(e) and 2(f) feature a multitude of different wavevectors distributed over all angles. The highest amplitudes are at low frequencies at low wavenumbers, reflecting some unordered base signal, which is modified by low amplitude, high-frequency components to describe the small grains, which were also found in Figs. 2(b) and 2(c). The FT of the perovskite layer on structured substrate [Fig. 2(e)] resemblances that of the flat perovskite layer on PTAA [Fig. 2(f)] much better that of the sinusoidal texture [Fig. 2(a)]. Hence, the hexagonal texture of the substrate is not transferred to the perovskite top surface.

As we now have established that spin coating allows for the fabrication of perovskite films of a high morphological quality on sinusoidally nanotextured substrates, we can proceed with the optical simulations of nanotextured perovskite–silicon tandem solar cells.

3 Simulation Details

3.1 Simulated Tandem Cell Architectures

For this study, we numerically investigated the three architectures shown in Fig. 3: Figure 3(a) shows the architecture with the "double-side" textured perovskite top cell. In Fig. 3(b), the "front side" architecture is shown, where the front interface of the perovskite absorber and all layers above are textured. In the "rear-side" textured architecture, Fig. 3(c), only the intermediate layers between the Si absorber and perovskite absorber are textured, whereas the interfaces on top of the perovskite layers remain flat. In all structures we assume conformal growth, meaning that all nanotextured interfaces have the same texture. For all architectures, we use a period of $P = 500$ nm, which is very well suited for solar cells.[22,23,40]

As we have seen in Sec. 2, spin-coating allows for the growth of perovskite layers on nanotextured substrates. These layers are almost flat on top and hence resemble the architecture with the rear-side texture shown in Fig. 3(c). As demonstrated by other groups, a front-side textured architecture can be realized with nanoimprint processes.[26–28] Paetzold and coworkers demonstrated that pattering the front surface does not affect the open circuit voltage V_{oc} and fill factors of solar cells.[26] One strategy to realize double-sided architectures is using vacuum deposition, which can lead to conformal growth of the perovskite layer.[41]

In detail, the perovskite top cells shown in Fig. 3 consist of a lithium fluoride (LiF) anti-reflective coating, an ITO front contact, a tin oxide (SnO_2) buffer layer, an electron-selective
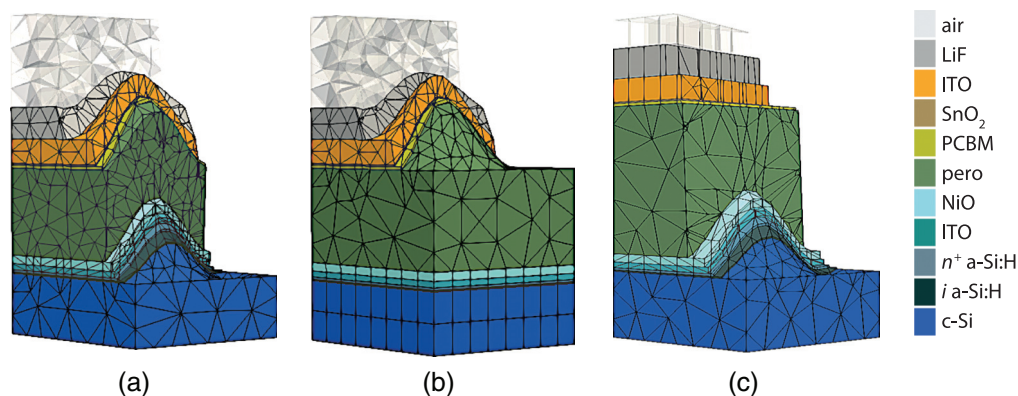

Fig. 3 Three different cell architectures with (a) double-side textured, (b) front-side textured, and (c) back-side textured perovskite top cell. For the FEM simulations, the simulation domains are enclosed by air and silicon halfspaces. The light is incident from the air half space (top). The thicknesses of the layers are shown in Table 1.

Table 1 The thicknesses of the layers in our simulated tandem cell. These are the set of optimal layer thicknesses numerically calculated in Ref. 42. The perovskite thickness has been adapted to take into account the different (n, k) data used in this work. The air and c-Si layer are treated as infinite half spaces in the simulation. All layer thicknesses except the one of the perovskite are kept constant during the simulation. All values are in nm.

LiF	ITO	SnO$_2$	PCBM	Perovskite	NiO	ITO	n^+ a-Si:H	i a-Si:H
107	80	5	15	333	10	20	8	5

phenyl-C61-butyric acid methyl ester (PCBM) contact layer, the perovskite absorber, a hole-selective nickel oxide (NiO) layer, and the ITO interconnecting layer.[12,13] The silicon bottom cell consists of n^+-doped and intrinsic (i) hydrogenated amorphous silicon (a-Si:H) layers and the c-Si wafer absorber, which is assumed to be infinitely thick in the finite-element method (FEM) simulations, as explained in Sec. 3.3. All other layers take their thicknesses from previous work on optimizing a planar tandem device[42] and are shown in Table 1.

3.2 Mathematical Description of Hexagonal Lattices

The hexagonal sinusoidal nanotextures are mathematically described with

$$f_{\text{hex}}(x, y) = -\frac{8}{9} \cos\left[\frac{1}{2}\left(x + \sqrt{3}y\right)\right] \cos\left[\frac{1}{2}\left(x - \sqrt{3}y\right)\right] \cos(x). \qquad (1)$$

We discussed them in detail in Ref. 22, where the texture described in Eq. (1) is referred to as "negative cosine." For the solar cells discussed in this work, we also tested the "positive cosine" textures and just as in Ref. 22, they are outperformed by the negative cosine textures. Therefore, we only report about solar cells with negative cosine textures in this article.

We can scale the nanotexture to the desired period P, which is the side length of the rhombus-shaped unit cell, with the following substitutions:

$$x \rightarrow \frac{2\pi}{\sqrt{3}P}x \quad \text{and} \quad y \rightarrow \frac{2\pi}{\sqrt{3}P}y. \qquad (2)$$

The valley-to-peak height h of the nanotexture can be set by multiplying (1) with h. The aspect ratio a is defined as $a = h/P$; small or large values of a lead to flat or steep textures, respectively.

3.3 Simulation Methods

The optical simulations are performed with the finite element method (FEM) solver JCMsuite,[43] which provides a rigorous solution to Maxwell's equations for a given structure. As shown in Fig. 3, the three-dimensional (3-D) structures are meshed using tetrahedral and prismoidal elements.

The complex refractive index spectra (n, k) used for the simulations were determined as follows: perovskite data were retrieved using ellipsometry and transmittance/reflectance spectrophotometry.[44] For NiO$_x$[45] and the sputtered ITO layers, ellipsometry and the program RIGVM were used.[46] Data for PCBM were extracted from reflectance/transmittance measurements with the method described in Refs. 47 and 48. The SnO$_2$ layers were deposited using plasma-enhanced atomic layer deposition and characterized with ellipsometry.[49] Data for the RF-PECVD a-Si:H layers[50] were extracted using SCOUT.[51] For LiF[52] and spiro-OMeTAD,[8] we used data from the literature.

We set the side-length constraint of the 3-D elements (prisms and tetrahedrals) for the FEM simulations to $\lambda/n(\lambda)$, where λ is the incident wavelength and $n(\lambda)$ is the refractive index of the material. In this way, one grid was generated for every wavelength interval of 100-nm width. Employing higher polynomial degrees (between 3 and 6) rather than finer meshes in an adaptive hp-FEM implementation allows to achieve accurate results at optimal computational costs.[53]
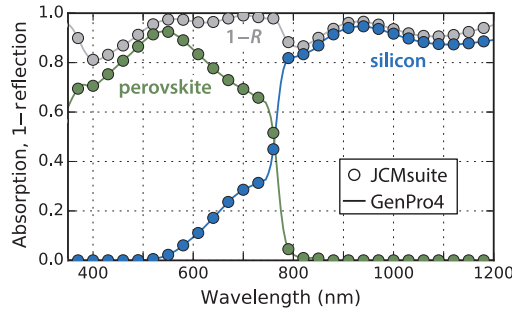
Fig. 4 Absorption spectra of the c-Si (blue) and the perovskite (green) layers and one minus the overall reflection (gray) for a planar reference structure with the layers as in Table 1 with an infinitely thick silicon layer. Results were computed with the FEM solver `JCMsuite` (circles) and the analytical tool `GenPro4` (lines).

A convergence study confirmed the accuracy of the pre-set accuracy value. To accurately reconstruct the sinusoidal interfaces, we set their surface side-length constraint to between 55 and 17 nm, depending on the aspect ratio. To obtain the angular dependence of the hexagonal unit cell, the azimuth of the incident wave is set to 0 deg and 30 deg and an average is taken.[22]

We model the c-Si absorber and the air layer as infinite half spaces, which is numerically realized using perfectly matched layers on the top and bottom boundaries. For the other faces of the computational domain, periodic boundary conditions are applied. Light is incident from the air half space.

To cross check the accuracy of the simulations, we compared simulations for the planar tandem device with `JCMsuite` (3-D FEM) and `GenPro4`, which can combine wave optics for coherent thin layers and ray optics for thick incoherent layers.[54] As can be seen in Fig. 4, the results obtained with the two methods are in excellent agreement.

However, the Si absorber of our tandem cell has a realistic thickness of 160 μm. To account for this, we approximate the absorption in the Si absorber by assuming that the rear side of the Si behaves as a Lambertian scatterer. In practice this means that the wavelength-dependent absorbtion coefficient of the infinite Si layer $\alpha(\lambda)$—which is obtained using the light transmitted into the Si in the FEM simulation—is converted to the absorption of a finite layer $A(\lambda)$ with Lambertian scattering using the the Tiedje–Yablonovitch limit

$$A(\lambda) = \frac{\alpha(\lambda)}{\alpha(\lambda) + (4[n(\lambda)]^2 L)^{-1}},\tag{3}$$

which is a function of the absorber thickness L, the wavelength-dependent absorption coefficient $\alpha(\lambda)$, and the wavelength dependent refractive index $n(\lambda)$.[55]

As a figure of merit, we use the photocurrent density J_{ph}, which can be calculated for the i'th layer from the absorption profile using

$$J_{\mathrm{ph},i} = -e \int_{310\ \mathrm{nm}}^{1200\ \mathrm{nm}} A_i(\lambda) \Phi_{AM1.5}(\lambda) \cos\theta_{in} \mathrm{d}\lambda,\tag{4}$$

where e is the elementary charge, $A_i(\lambda)$ is the absorption spectrum of the i'th layer, $\Phi_{AM1.5}(\lambda)$ is the spectral photon flux under AM1.5G condition,[56] and θ_{in} is the angle between the incident light and the solar cell normal. The photocurrent densities calculated for the perovskite and silicon layers are the maximum achievable current densities because we assume that all the absorbed light leads to the generation of electron-hole pairs, which are then extracted from the solar cell. The current densities for the other layers are losses due to parasitic absorption.

To estimate the potential power conversion efficiency of the tandem device, the open circuit voltage (V_{oc}) of each subcell and the fill factor (FF) of the overall device are required. Additionally, the logarithmic dependence of the V_{oc} on the photocurrent density must be taken into account. We assume the fill factor to be 81%.[57] Furthermore, we assume that a single junction perovskite and Si solar cell under standard illumination conditions have a short circuit current density of 22 and 42 mA/cm^2 with a related open circuit voltage of 1.130 and 0.730 V,
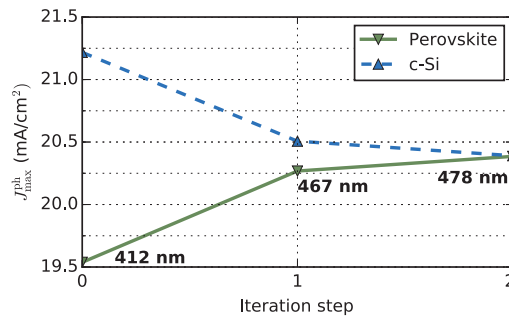
Fig. 5 Example for applying Newton's method to adapt the perovskite thickness for current matching. For the back-side textured structure with an aspect ratio of $a = 1.0$. The effective perovskite thickness after each iteration step using Newton's method is given; only two iterations are required to reach current matching.

respectively. These values will then be used to estimate the V_{oc} values for the subcells in the tandem device.

To determine the perovskite thickness for current matching, we use Newton's method. The method finds the roots of a function $f(x)$ with derivative $f'(x)$ beginning at an inital value x_0 and repeats the iteration

$$x_{n+1} = x_n - \frac{f(x_n)}{f'(x_n)},\qquad(5)$$

until a sufficient accuracy is reached. The partial derivatives of the absorption of the perovskite and c-Si absorber layers with respect to the perovskite layer thickness are computed directly in JCMsuite.[58]

As inital value for the architecture with the smallest aspect ratio, we choose a perovskite thickness of 333 nm, which is the optimal value for the planar architecture.[42] For each new value of aspect ratio, we use the optimized value for the previous aspect ratio as initial value. By employing this method, we reduce the number of simulations because no extensive thickness parameter scans are required. An example is shown in Fig. 5, where we see the current densities in the perovskite and silicon subcells after each iteration for the back side textured structure with aspect ratio $a = 1.0$. To reach current matching, the perovskite thickness had to be increased from 412 to 478 nm.

4 Simulation Results

Figure 6 shows the matched maximum achievable current density as a function of the aspect ratio a for the three architectures shown in Fig. 3. For all three textures, the largest aspect ratio leads to the maximum current densities, which are 21.3, 20.9, and 20.4 mA/cm^2 for the double-, front-,
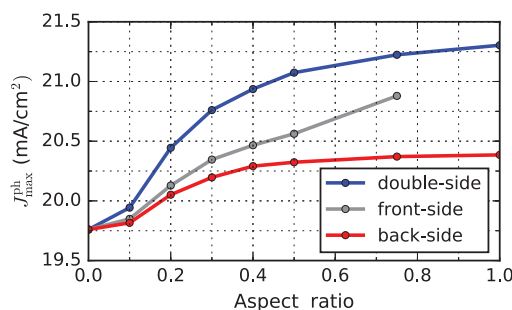

Fig. 6 The maximum achievable matched current density J_{ph}^{max} after thickness optimization shown in dependence of the aspect ratio for the three architectures shown in 3. The corresponding optimal effective perovskite layer thicknesses are shown in Table 2.

Table 2 The effective perovskite thicknesses of the three different architectures illustrated in Fig. 3 with various aspect ratios after thickness optimization for current matching. All values are in nm.

Aspect ratio	0.1	0.2	0.3	0.4	0.5	0.75	1.0
Double-side	333	340	343	350	360	378	386
Front-side	324	306	283	262	243	201	—
Back-side	338	364	386	402	411	439	478

and back-sided textures, respectively. For the double- and back-side textures that was $a = 1.0$, while for the front-side texture that was $a = 0.75$. An aspect ratio of 1.0 was not achievable with the front-sided texture because the layer thickness required for current matching would be smaller than the texture height. As discussed in Sec. 2, the architecture with the back-side textured solar cell (Fig. 6, red lines) is closest to the experimentally realizable architecture. Note that in this case the difference in the current densities J_{ph}^{max} between $a = 0.3$, 0.4, and 0.5 is <0.1 mA/cm^2.

The effective perovskite thicknesses d at current match conditions are shown in Table 2; d is the thickness a flat perovskite layer would have with the same volume and hence the same amount of material. The values are obtained by dividing the volumes of the perovskite absorber by the surface of the base. Comparing the effective thicknesses with the associated current densities we can see that a high effective thickness does not necessarily relate to a high absorption rate. For the architecture where only the layers above the perovskite absorber are textured (front-side), we find the highest proportion of absorption rate in the perovskite layer per effective thickness for all aspect ratios.

Starting from the photocurrent density and V_{oc} of single junction cells given in Sec. 3.3, the matched photocurrent density values for the planar tandem of 19.7 and 19.8 mA/cm^2 result in V_{oc} values of 1.127 and 0.711 V for the perovskite and Si subcells, respectively. This leads to a power conversion efficiency of 29.3%. The matched photo-current density for a device with a double-sided texture with $a = 1.0$ is 21.3 mA/cm^2, which results in V_{oc} values of 1.129 and 0.713 V for the perovskite and Si subcells, respectively, leading to a power conversion efficiency of 31.8%. This represents an increase in 2.5% efficiency absolute at the standard perovskite bandgap of 1.56 eV. For the realistic back-textured architecture, the matched current density is 20.3 mA/cm^2 at $a = 0.5$, leading to V_{oc} values of 1.128 and 0.711 V for the perovskite and Si cells, respectively. That results in an overall power conversion efficiency of 30.2%.

Figure 7 shows the absorption profile for silicon perovskite solar cells with (a) a planar and (b) a fully textured perovskite top cell with aspect ratio $a = 1.0$. Additionally, the corresponding
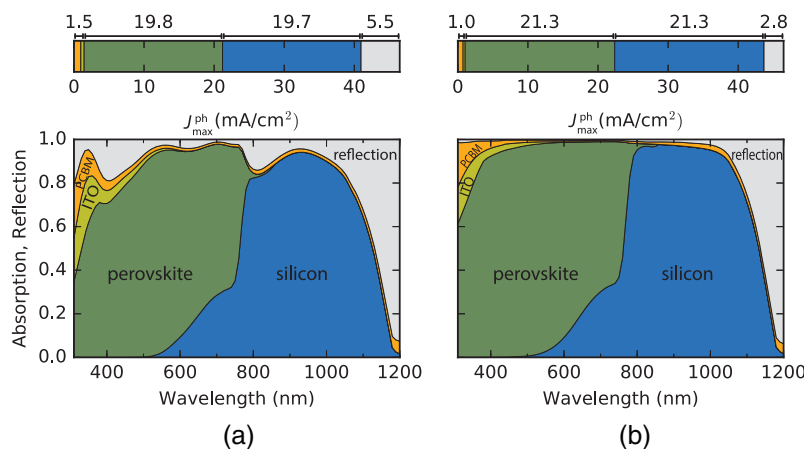

Fig. 7 Absorption profile and associated theoretical current density for the (a) planar and (b) fully textured architecture with $a = 1.0$. With a maximum achievable current density of 21.3 mA/cm^2 for each absorber cell, we have a power conversion efficiency of 31.8%.
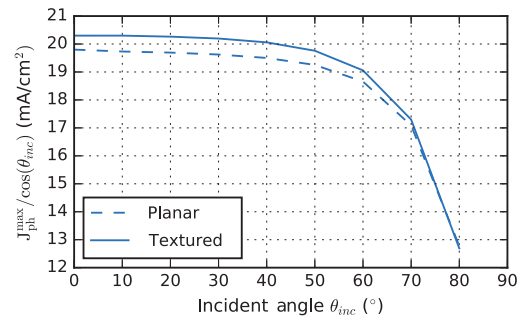
Fig. 8 The angular dependence of the maximum matched current density for the planar and back textured ($a = 0.5$) structure.

current densities are shown. Note that only the current densities from the perovskite and silicon layers can contribute to electricity generation, whereas the other values are parasitic absorption or reflection losses. For silicon, we assume Lambertian scattering at the back using Eq. (3). Compared with the planar architecture, an additional current density of about 1.5 mA/cm^2 per subcell can be collected by implementing the double-sided texture with $a = 1.0$.

We see that the planar device suffers from large reflective losses in the wavelength range from 400 to 1100 nm. These losses oscillate in magnitude, which is typical for Fabry–Perot type reflections from a planar thin-film layer stack. In contrast, the fully textured device shows negligible reflection losses in the same wavelength region. Hence, the overall reflection losses are reduced by 2.7 mA/cm^2. The sinusoidal texture scatters the light, thereby stopping multiple reflections necessary for Fabry–Perot oscillations, which is evident from the reflection curve being largely independent of wavelength. At the same time, the texture reduces the total reflection, which directly increases the absorption in the absorber layers.

The angular-dependent performance is also an important factor for solar cells without active tracking. Figure 8 shows how the maximum matched current density varies with the angle of incidence for both the optimized planar device and the back textured device with aspect ratio of 0.5. As the incident power falls off as $\cos(\theta_{\text{inc}})$, where θ_{inc} is the incident angle, we divide the maximum matched current density by this factor to highlight the angular-dependent difference in light absorption between the planar- and back-textured device, independent of the incident power. It can be seen that the advantage in absorption and therefore current density provided by the nanotexture is maintained over a wide-angle range up to 60 deg. This supports the application of sinusoidal nanotextures for solar applications.

5 Conclusion

In this work, we numerically studied nanophotonic light management concepts for perovskite–silicon tandem solar cells. As nanophotonic structures we used hexagonal sinusoidal nanotextures. To achieve current matching, we optimized the thickness of the perovskite absorber with Newton's method, which typically converged after only a single step. To experimentally motivate this numerical study, we demonstrated the deposition of perovskite layers onto sinusoidally structured nanophotonic substrates with spin coating.

The highest maximum achievable photocurrent density $J_{\text{ph}}^{\text{max}} = 21.3$ mA/cm^2 in each subcell was obtained with the fully textured structure with aspect ratio of $a = 1.0$, which corresponds to a power conversion efficiency of 31.8% at the standard perovskite bandgap. Compared with the planar architecture, we have an increase in $J_{\text{ph}}^{\text{max}}$ of 1.6 mA/cm^2 for each absorber layer and a potential increase of power conversion efficiency of 2.5% absolute. The efficiency can be increased even further using perovskite materials with higher bandgaps, where the optimal bandgap is around 1.7 eV.[13,57]

Future experimental efforts should focus on the implementation of double-side textured perovskite layers onto high-aspect-ratio substrates as well as to the experimental realization of textured perovskite single-junctions. Special care has to be taken to investigate the implications of structured substrates for perovskite crystal quality and thus electrical performance parameters

were neglected in this study. Ultimately, future efforts should be directed to fully textured and highly efficient perovskite–silicon tandem solar cells.

Appendix: Experimental Details

The PTAA layer for the perovskite reference sample is prepared by spin-coating 100 μL of a 2-mg PTAA (Aldrich) per mL of Toluene (Aldrich) solution onto an ITO-coated substrate (Automatic Research). After spin-coating at 4000 rpm for 30 s, the sample is annealed at 100℃ for 10 min.

For the mixed cation, mixed halide perovskite, two 1.5-M precursor solutions of PbI_2 (TCI) and $PbBr_2$ (TCI) in dimethylformamide (DMF, Aldrich) and dimethyl sulfoxide (DMSO, Aldrich) (4 : 1 $v : v$) are mixed with formamidinium iodide (FAI, Dyenamo) and methylammonium bromide (MABr, Dyenamo), respectively. The resulting $FAPbI_3$ and $MAPbBr_3$ solutions with a Pb-to-cation ratio of 1.09 : 1 are mixed in a 5 : 1 ($v : v$) ratio and supplemented by addition of 5 vol% of a 1.5 cesium iodide (CsI, abcr) in DMSO solution. This solution is then diluted down to a 0.8-M solution to obtain films in the desired thickness range. For this, DMF:DMSO 4 : 1 ($v : v$) is added to the as-prepared solution.

For fabricating the perovskite layers, the antisolvent method was used. For this, the perovskite precursor solution was spin-coated onto the different substrates at 1000 and 6000 rpm for 10 and 20 s, respectively. About 5 s prior to the end of process, 200 μL of chlorobenzene (Aldrich) was dripped as antisolvent. After this, the sample was directly transferred to a hot plate and baked at 100℃ for 1 h.

Acknowledgments

References

1. M. A. Green et al., "Solar cell efficiency tables (version 51)," *Prog. Photovolt. Res. Appl.* **26**, 3–12 (2018).
2. A. Richter, M. Hermle, and S. Glunz, "Reassessment of the limiting efficiency for crystalline silicon solar cells," *IEEE J. Photovolt.* **3**, 1184–1191 (2013).
3. M. A. Green, "Commercial progress and challenges for photovoltaics," *Nat. Energy* **1**, 15015 (2016).
4. W. Shockley and H. J. Queisser, "Detailed balance limit of efficiency of p-n junction solar cells," *J. Appl. Phys.* **32**, 510–519 (1961).
5. S. De Wolf et al., "Organometallic halide perovskites: sharp optical absorption edge and its relation to photovoltaic performance," *J. Phys. Chem. Lett.* **5**, 1035–1039 (2014).
6. G. E. Eperon et al., "Formamidinium lead trihalide: a broadly tunable perovskite for efficient planar heterojunction solar cells," *Energy Environ. Sci.* **7**, 982–988 (2014).
7. R. E. Beal et al., "Cesium lead halide perovskites with improved stability for tandem solar cells," *J. Phys. Chem. Lett.* **7**, 746–751 (2016).
8. M. Filipič et al., "$CH_3NH_3PbI_3$ perovskite/silicon tandem solar cells: characterization based optical simulations," *Opt. Express* **23**, A263–A278 (2015).

9. N. N. Lal, T. P. White, and K. R. Catchpole, "Optics and light trapping for tandem solar cells on silicon," *IEEE J. Photovoltaics* **4**, 1380–1386 (2014).

10. D. T. Grant et al., "Design guidelines for perovskite/silicon 2-terminal tandem solar cells: an optical study," *Opt. Express* **24**, A1454–A1470 (2016).

11. R. Santbergen et al., "Minimizing optical losses in monolithic perovskite/c-Si tandem solar cells with a flat top cell," *Opt. Express* **24**, A1288–A1299 (2016).

12. K. A. Bush et al., "23.6%-efficient monolithic perovskite/silicon tandem solar cells with improved stability," *Nat. Energy* **2**, 17009 (2017).

13. K. Jäger et al., "Numerical optical optimization of monolithic planar perovskite-silicon tandem solar cells with regular and inverted device architectures," *Opt. Express* **25**, A473–A482 (2017).

14. J. Gjessing, A. S. Sudbø, and E. S. Marstein, "Comparison of periodic light-trapping structures in thin crystalline silicon solar cells," *J. Appl. Phys.* **110**, 033104 (2011).

15. J. Grandidier et al., "Light absorption enhancement in thin-film solar cells using whispering gallery modes in dielectric nanospheres," *Adv. Mater.* **23**, 1272–1276 (2011).

16. C. Battaglia et al., "Light trapping in solar cells: can periodic beat random?" *ACS Nano* **6**, 2790–2797 (2012).

17. S. Mokkapati and K. R. Catchpole, "Nanophotonic light trapping in solar cells," *J. Appl. Phys.* **112**, 101101 (2012).

18. P. Spinelli et al., "Al_2O_3/TiO_2 nano-pattern antireflection coating with ultralow surface recombination," *Appl. Phys. Lett.* **102**, 233902 (2013).

19. A. N. Sprafke and R. B. Wehrspohn, "Light trapping concepts for photon management in solar cells," *Green* **2**, 177–187 (2013).

20. J. Eisenlohr et al., "Hexagonal sphere gratings for enhanced light trapping in crystalline silicon solar cells," *Opt. Express* **22**, A111–A119 (2014).

21. D. Ha et al., "Demonstration of resonance coupling in scalable dielectric microresonator coatings for photovoltaics," *ACS Appl. Mater. Interfaces* **8**, 24536–24542 (2016).

22. K. Jäger et al., "Simulations of sinusoidal nanotextures for coupling light into c-Si thin-film solar cells," *Opt. Express* **24**, A569–A580 (2016).

23. K. Jäger et al., "On accurate simulations of thin-film solar cells with a thick glass superstrate," *Opt. Express* **26**, A99–A107 (2018).

24. G. Köppel, B. Rech, and C. Becker, "Sinusoidal nanotextures for light management in silicon thin-film solar cells," *Nanoscale* **8**, 8722–8728 (2016).

25. G. Köppel et al., "Combining tailor-made textures for light in-coupling and light trapping in liquid phase crystallized silicon thin-film solar cells," *Opt. Express* **25**, A467–A472 (2017).

26. U. W. Paetzold et al., "Nanophotonic front electrodes for perovskite solar cells," *Appl. Phys. Lett.* **106**, 173101 (2015).

27. S. Brittman et al., "Controlling crystallization to imprint nanophotonic structures into halide perovskites using soft lithography," *J. Mater. Chem. C* **5**, 8301–8307 (2017).

28. N. Pourdavoud et al., "Photonic nanostructures patterned by thermal nanoimprint directly into organo-metal halide perovskites," *Adv. Mater.* **29**, 1605003 (2017).

29. S.-H. Lin et al., "Nanophotonic perovskite solar cell architecture with a three-dimensional TiO_2 nanodendrite scaffold for light trapping and electron collection," *J. Mater. Chem. A* **4**, 1119–1125 (2016).

30. J.-W. Lee et al., "Opto-electronic properties of TiO_2 nanohelices with embedded $HC(NH_2)_2PbI_3$ perovskite solar cells," *J. Mater. Chem. A* **3**, 9179–9186 (2015).

31. C. Becker et al., "5×5 cm^2 silicon photonic crystal slabs on glass and plastic foil exhibiting broadband absorption and high-intensity near-fields," *Sci. Rep.* **4**, 5886 (2014).

32. M. Jost et al., "Efficient light management by textured nanoimprinted layers for perovskite solar cells," *ACS Photonics* **4**, 1232–1239 (2017).

33. C. M. Wolff et al., "Reduced interface-mediated recombination for high open-circuit voltages in $CH_3NH_3PbI_3$ solar cells," *Adv. Mater.* **29**, 1700159 (2017).

34. M. Stolterfoht et al., "Approaching the fill factor Shockley–Queisser limit in stable, dopant-free triple cation perovskite solar cells," *Energy Environ. Sci.* **10**, 1530–1539 (2017).

35. M. Saliba et al., "Cesium-containing triple cation perovskite solar cells: improved stability, reproducibility and high efficiency," *Energy Environ. Sci.* **9**, 1989–1997 (2016).

36. H. Minemawari et al., "Inkjet printing of single-crystal films," *Nature* **475**, 364–367 (2011).

37. L. Kegelmann et al., "It takes two to tango—double-layer selective contacts in perovskite solar cells for improved device performance and reduced hysteresis," *ACS Appl. Mater. Interfaces* **9**, 17245–17255 (2017).

38. N. J. Jeon et al., "Solvent engineering for high-performance inorganic-organic hybrid perovskite solar cells," *Nat. Mater.* **13**, 897–903 (2014).

39. J. Kim et al., "Stable and null current hysteresis perovskite solar cells based nitrogen doped graphene oxide nanoribbons hole transport layer," *Sci. Rep.* **6**, 27773 (2016).

40. D. Eisenhauer et al., "Smooth anti-reflective three-dimensional textures for liquid phase crystallized silicon thin-film solar cells on glass," *Sci. Rep.* **7**, 2658 (2017).

41. C. Momblona et al., "Efficient vacuum deposited p-i-n and n-i-p perovskite solar cells employing doped charge transport layers," *Energy Environ. Sci.* **9**, 3456–3463 (2016).

42. K. Jäger et al., "Numerical optical optimization of perovskite-silicon tandem solar cells," in *Proc. of 33rd European Photovoltaic Solar Energy Conf. and Exhibition*, pp. 1057–1060 (2017).

43. J. Pomplun et al., "Adaptive finite element method for simulation of optical nano structures," *Phys. Status Solidi B* **244**, 3419–3434 (2007).

44. J. A. Guerra et al., "Determination of the complex refractive index and optical bandgap of $CH_3NH_3PbI_3$ thin films," *J. Appl. Phys.* **121**, 173104 (2017).

45. J. You et al., "Improved air stability of perovskite solar cells via solution-processed metal oxide transport layers," *Nat. Nanotechnol.* **11**, 75–81 (2016).

46. A. Pflug et al., "Optical characterization of aluminum-doped zinc oxide films by advanced dispersion theories," *Thin Solid Films* **455**–**456**, 201–206 (2004).

47. S. Albrecht, "Generation, recombination and extraction of charges in polymer: fullerene bulk heterojunction solar cells," PhD Thesis, Universität Potsdam (2014).

48. A. B. Djurišić et al., "Improved method for determination of optical constants of organic thin films from reflection and transmission measurements," *Appl. Opt.* **39**, 1174–1182 (2000).

49. G. Chistiakova et al., "In-system photoelectron spectroscopy study of tin oxide layers produced from tetrakis(dimethylamino)tin by plasma enhanced atomic layer deposition," *J. Vac. Sci. Technol. A* **36**, 02D401 (2018).

50. L. Mazzarella et al., "Nanocrystalline silicon emitter optimization for Si-HJ solar cells: Substrate selectivity and CO_2 plasma treatment effect," *Phys. Status Solidi A* **214**, 1532958 (2017).

51. W.Theiss, Hard- and Software, http://www.mtheiss.com (2002).

52. H. H. Li, "Refractive index of alkali halides and its wavelength and temperature derivatives," *J. Phys. Chem. Ref. Data* **5**, 329–528 (1976).

53. S. Burger et al., "Hp-finite-elements for simulating electromagnetic fields in optical devices with rough textures," *Proc. SPIE* **9630**, 96300S (2015).

54. R. Santbergen et al., "GenPro4 optical model for solar cell simulation and its application to multijunction solar cells," *IEEE J. Photovoltaics* **7**, 919–926 (2017).

55. T. Tiedje et al., "Limiting efficiency of silicon solar cells," *IEEE Trans. Electron. Devices* **31**, 711–716 (1984).

56. "IEC:60904-3: photovoltaic devices—part 3: measurement principles for terrestrial photovoltaic (PV) solar devices with reference spectral irradiance data," International Electrotechnical Commission (2008).

57. S. Albrecht et al., "Towards optical optimization of planar monolithic perovskite/silicon-heterojunction tandem solar cells," *J. Opt.* **18**, 064012 (2016).

58. S. Burger et al., "Fast simulation method for parameter reconstruction in optical metrology," *Proc. SPIE* **8681**, 868119 (2013).

Duote Chen studied physics at the Freie Universität Berlin from where she received a bachelor's degree in 2016. Currently, she studies medical physics at the Beuth University of Applied Sciences Berlin. She conducted the work presented in this paper as a research assistant at Helmholtz–Zentrum Berlin.

Phillip Manley completed a master's degree in physics at Durham University in 2012. He went on to complete a doctorate in physics at the Freie Universität Berlin in cooperation with the Helmholtz–Zentrum Berlin in 2016 on the topic of nanoplasmonics for solar energy. He now works at the Helmholtz–Zentrum Berlin continuing to work on light management for solar energy.

Philipp Tockhorn is currently a PhD student at Helmholtz–Zentrum Berlin, working on the optimization of perovskite solar cells for the application in monolithic perovskite–silicon tandem solar cells. Before that, he studied physics at the Freie Universität Berlin and at the University of Amsterdam with a focus on photovoltaics and other renewable energy technologies.

David Eisenhauer studied physics at Heidelberg University and Technische Universität Berlin. He is currently a doctoral researcher at Helmholtz–Zentrum Berlin, where his research focusses on the development of tailored nanostructures for thin-film silicon solar cells and perovskite–silicon tandem solar cells.

Grit Köppel studied natural sciences in the Information Society at the Technische Universität Berlin and material science and engineering at Kiel University, where she completed a master's degree in 2013. In 2017, she received his PhD at Technische Universität Berlin for her work on "Liquid phase crystallized silicon on sinusoidal textured glass substrates," which she conducted at Helmholtz–Zentrum Berlin.

Martin Hammerschmidt received his Diploma in applied mathematics from the Technical University of Munich in 2011 and his PhD in the same field from the Freie Universität Berlin in 2016. His research interests include advanced finite element techniques, model order reduction methods and their applications in rigorous nano-optical simulations of photonic devices with a focus on energy harvesting devices.

Sven Burger leads the Computational Nano Optics Group at Zuse Institute Berlin. He also holds a position at JCMwave GmbH. He graduated in physics at the Leibniz Universität Hannover, where he also received a PhD in experimental physics. He further was a postdoctoral researcher at the European Laboratory for Nonlinear Spectroscopy in Florence and a lecturer at Technische Universität Berlin.

Steve Albrecht leads a young investigator group for perovskite-based multijunction photovoltaics at Helmholtz–Zentrum Berlin. He received a PhD in physics from the University of Potsdam. For his work on organic solar cells he was awarded with the Carl–Ramsauer–Prize and the Young Researcher Prize of the Berlin Physical Society and the Leibniz–Kolleg Potsdam, respectively. In 2014, he joined at Helmholtz–Zentrum Berlin as a postdoc until his young investigator group was founded.

Christiane Becker studied physics at the University of Karlsruhe and Heidelberg University, from where she obtained her diploma (MSc) in physics with distinction. After graduation as a PhD from University of Karlsruhe in 2006, she joined Helmholtz–Zentrum Berlin. Since 2012 she is head of the Nanostructured Silicon Group. She received an appointment as a professor at the University of Applied Sciences HTW Berlin in 2014. Her research primarily focusses on silicon nanostructures for photovoltaic and photonic applications.

Klaus Jäger received his diploma (MSc) as a physicist from the Swiss Federal Institute of Technology Zurich in 2008. In 2012, he graduated as a PhD with distinction from Delft University of Technology. After working in industry and a research position at Delft University of Technology, currently, he is a senior scientist at the Helmholtz–Zentrum Berlin. His research activities lie primarily with optical simulations for solar energy.